Journal of Materials Chemistry A

Deposition Condition Impacts Charge Tunneling and Thermoelectric Properties of N-Heterocyclic Carbene Monolayers

Journal:	*Journal of Materials Chemistry A*
Manuscript ID	TA-ART-04-2023-002443.R1
Article Type:	Paper
Date Submitted by the Author:	28-Jun-2023
Complete List of Authors:	Kang, Hungu; Korea University, Chemistry Jang, Jiung; Korea University, Chemistry Kong, Gyu Don; Korea University, Chemistry Jung, Sangmin; Korea University, Chemistry Ohto, Tatsuhiko; Nagoya University, Materials Design Innovation Engineering Yoon, Hyo Jae; Korea University, Chemistry

SCHOLARONE™
Manuscripts

Deposition Condition Impacts Charge Tunneling and Thermoelectric Properties of N-Heterocyclic Carbene Monolayers

Hungu Kang,[a]† Jiung Jang,[a]† Gyu Don Kong,[a]† Sangmin Jung,[a] Tatsuhiko Ohto*[b] and Hyo Jae Yoon*[a]

†These authors contributed equally to this work.

[a] Department of Chemistry, Korea University, Seoul, 02841, Korea

[b] Department of Materials Design Innovation Engineering, Nagoya University, Furo-cho, Chikusa-ku, Aichi 464-8603, Japan

Corresponding Authors' E-mails: ohto@nagoya-u.jp (T.O); hyoon@korea.ac.kr (H.J.Y.)

Abstract

N-Heterocyclic carbene (NHC) is an emerging anchor moiety for surface engineering and various applications. While various deposition conditions have been reported, how these affect the charge transport properties of NHC adsorbates remains uncertain. A NHC salt precursor based on benzo[d]imidazole with a PF_6^- counterion was deposited onto an ultrasmooth gold substrate using three different conditions for creating NHC monolayers: ambient incubation (AI), base (tert-butoxide)-induced deprotonation (BD), and electrochemical deprotonation (ED). Junction measurements using the EGaIn technique revealed that current density increased by $\sim 10^{1.7}$ in the order of AI < BD < ED, while the Seebeck coefficient showed the opposite trend, ranging from 9.3 to 13.5 μV/K. First-principles calculation reproduced the experimentally observed positive sign of the Seebeck coefficient. Further surface characterizations and computational calculations indicated that the different deposition conditions cause variation in surface coverage in the order of AI < BD < ED. This variation has a significant influence on the broadening of HOMO level and marginal impact on the energy offset between HOMO and Fermi levels, accounting for the opposite trends of electrical conductance and thermopower as a function of the deposition conditions. Finally, we found that the power factor of the NHC monolayer can increase by $\sim 10^2$ depending on the deposition condition.

Keywords: N-heterocyclic carbene (NHC) • Deposition conditions • Self-assembled monolayer (SAM) • Tunneling • Thermoelectric

Introduction

The N-heterocyclic carbene (NHC) ligand forms a robust covalent bond with various transition metals, making it a felicitous choice as an anchor[1-6] for tightly attaching molecules to substrates in a range of applications including biosensing,[7] electrocatalysis,[8] electronics,[5, 9-14] thermoelectrics,[4, 15, 16] and therapeutics.[17] Compared to thiol, which is widely used to deposit organic molecules onto coinage metal surfaces to build self-assembled monolayers (SAMs), NHC can offer an alternative due to the easily oxidizable nature of the sulfur atom in thiol.[18-20] In contrast, the NHC-metal bond is stronger than the traditional thiol-metal bond[21-24] and produces a sulfur-free interface, ensuring long-term stability under thermal, chemical, and photochemical conditions.[2, 13, 15]

In typical molecular deposition using a thiol anchor, no additives are needed.[20, 25, 26] However, the bare NHC molecule has two unshared valence electrons on its carbenic carbon atom, making it highly reactive. Therefore, salt or zwitterion precursors, such as imidazolium salts, are widely employed to create reactive NHC species that can covalently bond with surface exposed metal atoms.[2, 7, 21, 27-30] To generate the reactive carbene species, a carbenic proton in the salt precursor must be deprotonated. The salt precursors can be deposited to create SAMs under three different conditions: i) ambient incubation (AI) like the traditional thiol anchor method,[7, 13] ii) base-induced deprotonation (BD) of the carbenic proton,[27, 29] and iii) electrochemical deprotonation (ED).[5, 27] **Figure 1a-c** summarizes these conditions. In addition to solution-phase deposition, NHC monolayers can also be formed by vapor deposition in ultrahigh vacuum conditions.[7, 21, 30-32]

A handful of studies have reported the potential of the NHC anchor for constructing molecular-scale electronic devices.[4, 5, 13, 15, 16] Despite these stimulating findings, it remains uncertain how different deposition conditions affect the charge tunneling and thermoelectric properties of NHC adsorbates. In this work, we fabricated SAMs with an NHC precursor

bearing benzo[d]imidazole backbone and PF_6^- counterion on ultrasmooth template-stripped gold (Au^{TS})[4, 33] (**Figure 1d, e**) using the three different solution-phase deposition conditions: AI, BD, and ED. We evaluated their charge transport performances using the junction technique based on eutectic Ga-In (EGaIn).[33-36] Our results showed that the tunneling current density (*J*, A/cm^2) at +1.0 V increases by up to 1.7 orders of magnitude in the order of AI < BD < ED, while the Seebeck coefficient (*S*, μV/K) decreases in the opposite order of AI > BD > ED. The tunneling conductivity (σ, S/cm) increased by up to $10^{2.3}$ in the order of AI < BD < ED, leading to significant enhancement of power factor (PF= σS^2, $\mu W \cdot m^{-1} \cdot K^{-2}$) by ~$10^2$ times for the NHC SAM fabricated under the ED condition compared to the analogous SAM fabricated under the AI condition. Further experiments and quantum-chemical calculations indicated that the surface coverage variations, caused by the different deposition conditions, governed the work function of electrode and the molecule-electrode coupling strength, which accounted for the observed trends of *J*, *S*, and PF.

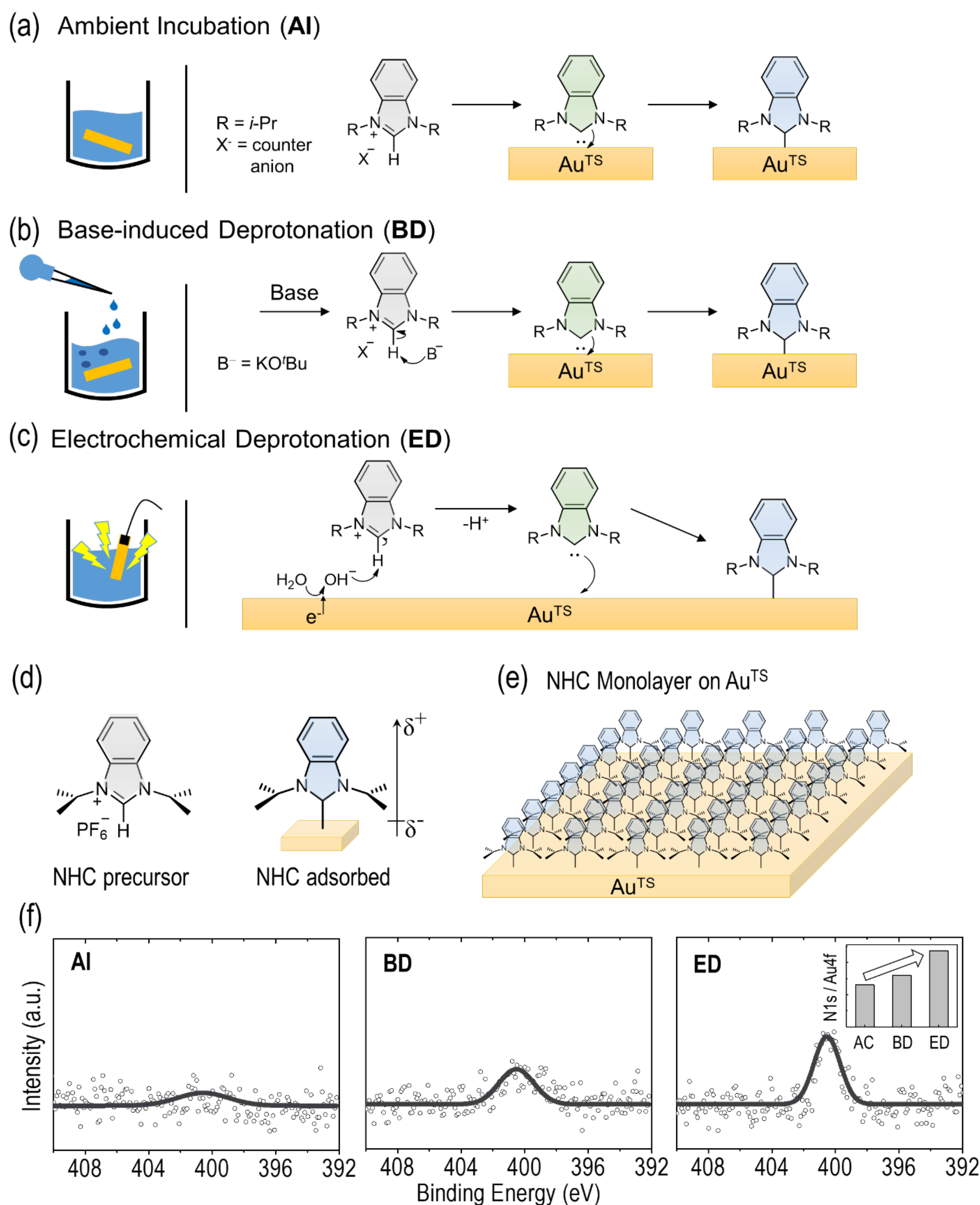

Figure 1. Schematic description of three different deposition conditions with NHC salt precursors: (a) ambient incubation (AI), (b) base-induced deprotonation (BD), and (c) electrochemical deprotonation (ED). (d) The NHC precursor we used in this work and its surface dipole for the adsorbate. (e) Schematic illustration of NHC SAM on Au^{TS}. (f) High-resolution X-ray photoelectron spectra for nitrogen (N 1s) atom for the NHC SAMs prepared in the AI, BD, and ED conditions. The inset compares the relative intensity of N 1s peak for the SAMs.

Results and Discussion

The NHC-PF_6 salt precursor[7, 37] and SAM[7, 27, 28] were prepared following the previously reported procedures. For the AI condition, a freshly prepared Au^{TS} chip (1 cm × 1 cm) was incubated in an ethanol solution containing a 3 mM NHC precursor at ambient conditions for 12 hrs. In the BD condition, we added 6 mM of potassium tert-butoxide (KO*t*-Bu) to the same solution used in the AI condition and left the resulting mixture for 2 hrs before incubating the freshly prepared Au^{TS} chip in the solution in an N_2-filled glovebox for 12 hrs. In the ED condition, we constructed a conventional three-electrode cell consisting of Ag/AgCl as the reference electrode, a Pt wire as the counter electrode, and an NHC-coated Au^{TS} chip as the working electrode. Electrochemical surface deposition was conducted in a solution containing 0.1 M tetrabutylammonium tetrafluoroborate and 5 mM NHC precursor in a mixture of water and acetonitrile (1:1000, v/v) with a voltage of -1.0 V applied to the cell for 2 mins. After the deposition process, we thoroughly rinsed the NHC-coated Au^{TS} chips with pure ethanol, followed by a 1-min flow of N_2 for all three deposition conditions.

XPS Analysis. The C 1s peak was deconvoluted into two peaks at 284.8 and 286.3 eV, corresponding to C-C/C=C and C-N, respectively, confirming the formation of NHC SAMs (**Figure S3-S5** in the Supporting Information). All SAMs, irrespective of deposition conditions, showed that the C 1s signal (284.8 eV) corresponding to C-C/C=C bonds was ~0.7 eV higher than that in typical aromatic thiol SAMs (284.1 eV). This could be attributed to the electrostatic effect resulting from a charge rearrangement at the molecule-metal interface.[13] The observed shift of C 1s peak could be attributed to the upward dipole moment of the NHC SAM with respect to the Au surface (**Figures S3-S5**), resulting from a significant charge transfer from the lone pair electron of the carbene carbon to the Au via σ-donation.

Figure 1f presents the high-resolution XPS spectra of N 1s for the SAMs. We found that the averaged value of N 1s peak integration for each deposition condition increased in the order

of AI < BD < ED (**Figure 1f**). The N 1s/Au 4f peak intensity ratio of SAM formed in the ED condition was 1.81- and 1.47-fold higher than those formed in the AI and BD conditions, respectively (inset in **Figure 1f**), indicating that the surface coverage of the NHC SAM increased in the order of AI < BD < ED. Our findings are consistent with those of Amit *et al.*[27] who compared the surface coverage of NO_2-functionalized NHC SAMs formed in different conditions using the XPS peak integration ratio of N 1s/Au 4f. The NHC SAM formed in the ED condition was 2.8-fold higher than that formed in the BD condition.[27] We did not detect the PF_6^- counterion in any of the SAMs, which is plausible given that PF_6^- is a non-coordinating anion that interacts weakly with cationic species due to its poorly nucleophilic character.

We determined the relative trend of the thickness of the SAM by comparing the Au 4f peak intensity[38, 39] between SAM-bound and bare Au substrates. The thickness of the NHC SAMs increased in the order of AI (1.16 nm) < BD (1.22 nm) < ED (1.24 nm). Our results are consistent with the literature values, which reported the thickness of the NHC SAM with methyl side group to be ~1.1 nm, estimated by XPS analysis.[13, 21] However, the surface coverage of our SAMs differed between deposition conditions, and the determination of SAM thickness using XPS relies on the decay of Au 4f peak intensity by the SAM. The decay can vary according to two factors: molecular tilt angle or surface coverage. NHC molecules with *i*-Pr side groups are known to have mostly upright geometries, even at low surface coverages.[21] Therefore, our trend implies that a more loosely packed SAM leads to less decay of Au peak intensity, and the trend is dominated by the surface coverage.

Electrochemical Impedance Spectroscopy (EIS). To confirm the difference in surface coverage between the NHC SAMs and measure the degree of defective pinholes within them, we utilized the EIS technique, known for its excellent sensitivity in quantifying SAM defects. The Bode phase plot reveals that the phase angle ($-\varphi_{1.0\ Hz}$) value at 1 Hz approaches 90° as the packing quality of the SAM improves.[40, 41] As illustrated in **Figure 2a** and **b**, the $-\varphi_{1.0\ Hz}$ value

followed the order of AI (36°) < BD (70°) < ED (71°), indicating that the ED condition produced the most densely packed SAM, while the AI condition resulted in the SAM with the most pinholes.[40, 42] The EIS spectra of SAMs followed the simple Randles' model, in which the double-layer capacitance is replaced by constant phase element (CPE).[43-45] The resistance of our NHC SAM (R_{SAM}, which reflects the movement of ion/water molecules within the SAM) was determined by an equivalent circuit: 1.8×10^5, 4.5×10^5, and 5.6×10^5 Ω for the AI, BD, and ED conditions, respectively. For comparison, the resistance of decanethiol (SC_{10}) SAM with ~1 nm thickness shows R_{SAM} value of 4.2×10^5 Ω.[41] The trend of R_{SAM} is consistent with the surface coverage trend determined by XPS. The percent electrochemically active surface area (%EAS) analysis was also consistent with the EIS data. The %EAS is defined as the ratio of reduction currents between the SAM-bound and bare electrodes, providing a relative comparison of the degree of structural defect between SAMs.[46, 47] Higher %EAS values indicate significant defects in a monolayer, whereas lower %EAS values indicate tightly packed molecules on the surfaces with a small degree of defects. As shown as **Figure S6**, the %EAS decreased in the order of AI (71 %) < BD (67 %) < ED (54 %), indicating that the AI and ED conditions led to the SAMs with the most and least pinhole defects, respectively.

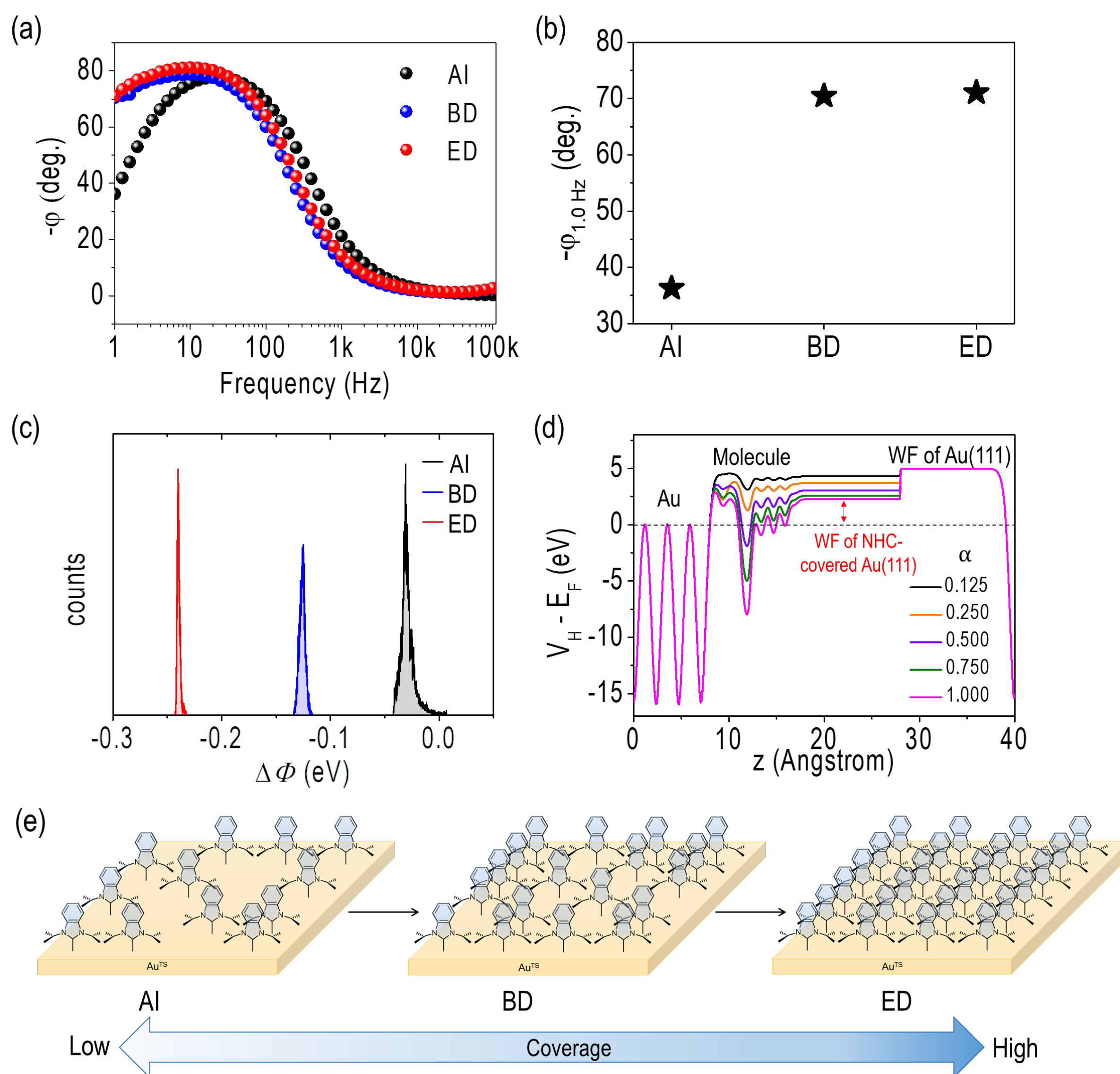

Figure 2. (a) Bode phase plots for the NHC SAMs depending on different fabrication methods. (b) Plot of phase values at 1.0 Hz ($-\varphi_{1.0\ Hz}$) as a function of the three conditions (AI, BD, and ED) to prepare NHC SAM. (c) The histograms showing the work function change ($\Delta\Phi$) of NHC SAM-bound Au substrates prepared by the different conditions. (d) Computational calculation of work function changes at varying the coverage of NHC molecules, using Hartree potential profile along the surface normal direction of the NHC SAM-coated Au(111) slab models. (e) Schematic describing the surface coverage difference for the SAMs prepared by the different conditions.

Kelvin Probe Force Microscopy (KPFM). The NHC SAM leads to a reduced work function (WF) of the Au surface due to the considerable charge transfer from the carbene carbon to the Au substrate.[13, 48] The dipole orientation of the NHC SAM is upward, in contrast to the thiolate SAM.[13] The NHC SAM can achieve a broader range of work function variation, up to 2.0 eV, which is higher than that of the thiolate SAM.[49] The equation below is used to express the WF change after SAM formation:[49]

$$\Delta\Phi = \frac{N\mu cos\theta}{\varepsilon\varepsilon_0} \qquad (1)$$

Here, N represents the density of molecules, μ is the dipole moment of the molecule, θ is the molecular tilt angle, ε is the effective dielectric constant of film, and ε_0 represents the permittivity of free space. Considering that the same NHC molecule was utilized for SAM preparation, the tilt angle of the molecule would be similar for the SAMs produced in the three conditions, and all three SAMs rarely contained PF_6^- counterion (according to the XPS analysis), we could hypothesize that the degree of WF reduction is mainly governed by surface coverage.[49] **Figure 2c** shows the histograms of the extent of WF reduction (ΔΦ) relative to bare gold, as determined by KPFM measurements. The data show that the WF varied from 4.87 to 4.66 eV and that the value of $\Delta\Phi$ increased in the order of AI (-0.03 eV) < BD (-0.12 eV) < ED (-0.24 eV), supporting our hypothesis and consistent with the surface coverage trend.

DFT Calculation of Work Function-Coverage Relationship. To further validate the experimentally observed correlation between WF changes and surface coverage, we performed density functional theory (DFT) calculations for the Au(111) surface coated by NHC SAMs (see the Supporting Information for details). The fully packed structure of the NHC SAM was adopted from a literature and top views of the structures employed for the calculations are shown in **Figure S7**.[21] The calculations indicated that, as the surface coverage (α) varied from 1.000 (fully packed) to 0.750, 0.500, 0.250, and 0.125, $\Delta\Phi$ relative to the bare Au(111) was

gradually reduced from -2.61 to -2.30, -1.85, -1.20, -0.65, respectively (**Figure 2d** and **Figure S8** in the Supporting Information). This calculation trend, where the WF decreases by increasing the coverage, concurred well with the trend observed in the experiment. The $\Delta\Phi$ derived from the computational calculations was larger than the experimentally determined one.[50] Such an overestimation may originate from the ideal orientations of molecules and the completely flat surface employed for the computational modeling and strong charge transfer between the molecule and substrate that are typically overestimated with DFT calculations.[50, 51] Ultimately, the XPS, EIS, and KPFM analyses, along with DFT calculations, suggest that the deposition conditions play a critical role in determining the surface coverage of NHC monolayers (**Figure 2e**), which directly impacts the degree of defective pinholes and the WF reduction.

Tunneling Current Density. We found that the deposition conditions have a dominant impact on the tunneling performance of NHC SAM. Using the EGaIn top-electrode, we collected current density (J, A/cm^2)-voltage (V, V) traces and created histograms of log|J| from which mean ($\mu_{\log|J|}$) and standard deviation ($\sigma_{\log|J|}$) were extracted. Regardless of the deposition condition, all the histograms displayed a log-normal distribution of J and were fitted to single Gaussian curves. **Figure 3a** and **b** depict log|J|-V plots and log|J(+1.0V)| histograms for the SAMs produced with NHC-PF_6^- precursor under different conditions. The log|J| increased in the order of AI < BD < ED: the log|J(+1.0 V)| in the AI condition was measured to be -1.0, which increased to +0.6 (by ~40 times in J) upon the change in the deposition condition to the ED. The yield of working junction was also significantly influenced by the deposition condition. The yield for the AI, BD, and ED conditions was 45, 78, and 94%, respectively (see the Supporting Information for details). The high yield of working junction in the SAM of the ED condition could be attributed to a high surface coverage of SAM, which reduces the probability of electrical short caused by defects. The value of $\sigma_{\log|J|}$ for the SAM formed in the AI condition

was noticeably larger than those for the SAMs formed in the BD and ED conditions, implying that the AI condition afforded the SAM that is relatively disordered. All these analyses were consistent with the trend of surface coverage, indicating that the $J(V)$ of the NHC SAM depends predominantly on the SAM quality, such as surface coverage, which is in turn dominated by the deposition condition. Although the NHC SAMs exhibited small rectification ratios, the rectification ratio—the degree of asymmetric feature in the J-V curve—increased in the order of AI (2.2) < BD (4.3) < ED (4.4). The occurrence of a small rectification ratio and a slight increasing trend may be attributed to the effect of deposition conditions on the work function and molecule-electrode coupling strength (see below for details).

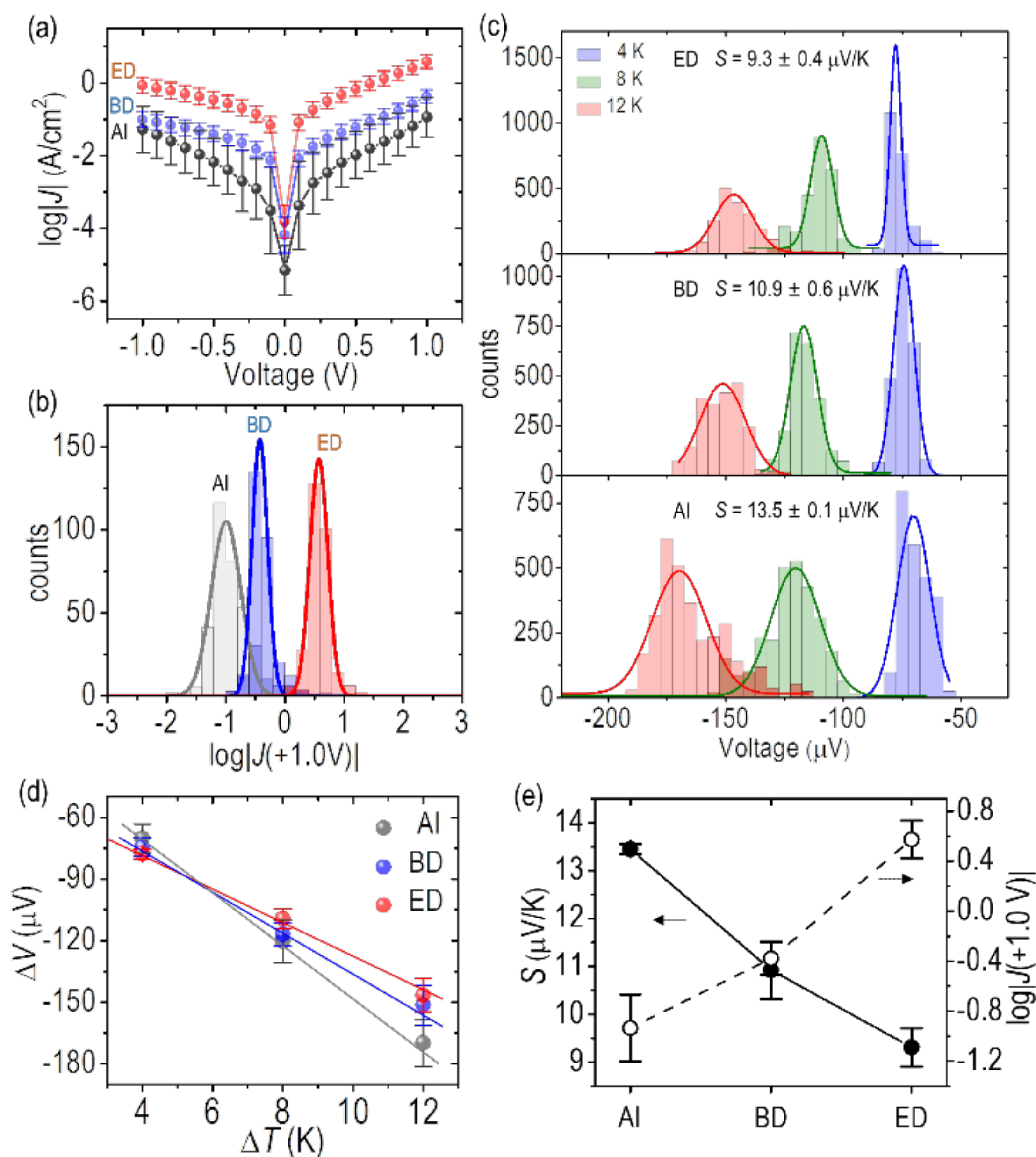

Figure 3. (a) Plots and (b) histograms of log10-scale tunneling current density (J, A/cm^2) against external voltage (±1.0 V) for SAMs formed with NHC-PF_6- precursor in the AI, BD, and ED conditions. Mean values of log|J(+1.0V)| estimated by the single Gaussian fitting curves to the histograms are -1.00, -0.43, and 0.57 for AI, BD, and ED, respectively. (c) Histograms of thermovoltage (ΔV, μV) for Au^{TS}/NHC//Ga_2O_3/EGaIn junctions. (d) Plots of ΔV as a function of ΔT. (e) Plots of S and log|J(+1.0V)| values as a function of deposition conditions.

Seebeck Coefficient. The Seebeck coefficient (S, μV/K) is defined as follows: $S = -\Delta V/\Delta T$ where ΔV (μV) is thermovoltage and ΔT (K) is temperature differential created across the junction (**Figure S12** in Supporting Information). Our study focused on the moderate temperature range ($\Delta T = 4$, 8, and 12 K) to avoid undesired thermal degradation of the organic molecule.[15, 52] Our previous study indicates there is no significance difference in temperature differential applied to a junction for air and vacuum condition when the temperature differentials are moderate ($\Delta T < \sim 20$ K).[53] Contribution from non-molecular components (e.g., the metal electrodes) to the total thermopower was considered for extracting the Seebeck coefficient of SAM from the total thermopower of junction following the previously reported procedures (**Figure S12c**).[54-56] Recent studies have indicated that S value of SAM can be reliably and reproducibly measured with the EGaIn technique.[4, 15, 16, 57] **Figure 3c** and **d** present histograms of ΔV and plot of ΔV against ΔT. The variation of ΔV ($\sigma_{\Delta V}$) in the ΔV histogram increased in order of AI > BD > ED. For instance, the values of $\sigma_{\Delta V}$ at $\Delta T = 12$ K were 11.5, 9.7, and 8.1 in AI, BD, and ED conditions, respectively. The distribution of ΔV is affected by the degree of molecular packing within a SAM,[16] and our observation could be due to the dependence of surface coverage of SAM on the deposition conditions. Regardless of the deposition conditions, all the NHC SAMs exhibited that, as ΔT increased, ΔV increased toward a negative value and yielded positive S values. The positive S values indicate the highest occupied molecular orbital (HOMO) dominates the transport in molecular junctions.[4] Interestingly, the value of S linearly decreased in the order of AI (13.5 ± 0.1 μV/K) > BD (10.9 ± 0.6 μV/K) > ED (9.3 ± 0.4 μV/K), which was opposite to the J trend (**Figure 3e**).

Calculation of Transport Channel. The dominant transport channel of the NHC molecular junction has been reported to be LUMO,[12] while positive S values are observed in our experiments, indicating that the transport is dominated by HOMO. To investigate the origin of

the positive sign of *S*, we performed first-principles transport calculations for the Au-NHC SAM-Au junction as well as the junction where the work functions of two electrodes are different, reflecting the experimental situation. Because the atomic positions of liquid metals cannot be determined, we approximated the top EGaIn electrode with Al(111). Al(111) has a similar work function (4.24 eV) with EGaIn (4.1-4.2 eV),[58, 59] and hence is able to model the potential profile of the real junction. The transport calculation results shown in **Figure S13** indicated that LUMO is closer to the Fermi level than HOMO in the Au-NHC SAM-Au junction, consistent with the literature result,[5, 12, 14] and anticipates a negative Seebeck coefficient. In contrast, the Au-NHC SAM-Al junction exhibits proximity of HOMO to the Fermi level and gives a positive Seebeck coefficient, which is due to the upward shift of molecular orbitals induced by the low work function of the Al electrode. Our calculations account for the positive *S* values observed in our experimental measurements for NHC SAMs and indicate HOMO as the dominant transport channel, which are attributed to the combination of Au and EGaIn as the bottom and top electrodes, respectively.

Transition Voltage Spectroscopy (TVS). Charge transport across molecular tunnel junction can be explained by a simple transmission function, $T(E)$, based on single Lorentzian-shaped energy level:

$$T(E) = \frac{\Gamma^2}{(E - E_{MO})^2 + \Gamma^2/4} \qquad (2)$$

This function indicates that tunneling probability is governed by energy offset (ΔE) between Fermi level (E_F) and accessible molecular orbital (E_{MO}) of Lorentzian shape, and the broadening of the MO (Γ).[57] The combination of transmission function with the Mott formula explains the *S* value of molecular junction:[57]

$$S = \frac{\pi^2 k_B^2 T}{3e} \frac{\partial \ln T(E)}{\partial E}\bigg|_{E=E_F} \qquad (3)$$

where k_B is the Boltzmann constant, T is the junction temperature, and e is the electron charge. This equation suggests that the gradient of $\ln(T(E))$ at E_F corresponds to S value, and ΔE and Γ play an important role in thermopower of junction.[57] TVS is a useful technique to extract ΔE and Γ values from an operating junction. The transition voltage, V_t, referring to the specific voltage that minimizes the Fowler-Nordheim plot ($1/V$ vs. $\ln(J/V^2)$), is related to ΔE and Γ.[60-62] The Fowler-Nordheim plots of our NHC SAMs are shown in **Figure S14** in the Supporting Information. We used the analytical single level model (SLM) formula derived from the Landauer picture[61, 63] and predicted current-voltage (I-V) characteristics with eq. 4:

$$I = GV\frac{\Delta E^2}{\Delta E^2-(eV/2)^2} \qquad (4)$$

where G is the zero bias conductance that can be described as follows

$$G = NG_0\frac{\Gamma^2}{\Delta E^2} \qquad (5)$$

Here, $\Gamma = \sqrt{\Gamma_s\Gamma_t} = \Delta E\sqrt{G/NG_0}$ is the average interface coupling (Γ_s and Γ_t are molecular coupling to the substrate (s) and the tip (t), $G_0 = 2e^2/h$ is the quantum conductance, and N is the number of molecules in the junctions). Since the focus of our study is on SAM (i.e., ensemble of molecules) and the surface coverage varies depending on the deposition conditions, we found that a qualitative ratio of N, rather than absolute values, was sufficient for explaining relative trends of J and S. In TVS analysis, we kept the EGaIn contact area relatively constant (approximately 1.18×10^9 nm^2) across the SAMs. Two NHC molecules are adsorbed per 1 nm^2 area for SAM formed in the AI condition.[21] Based on this, we estimated the number of NHC molecules occupying the junction area of 1.18×10^9 nm^2 to be 2.3×10^9. We roughly estimated the number of molecules for the other two SAMs (2.8×10^9 and 4.4×10^9 for the BD and ED conditions, respectively) by considering the XPS data (the ratio of N 1s to Au 4f peak intensity). The value of ΔE can be extracted according to eq. 6:

$$\Delta E = \frac{\sqrt{3}e|V_t|}{2} \qquad (6)$$

where V_t is transition voltage and assume that V_t is equal to $V_{t-} \approx V_{t+}$ for molecular junctions.

The absolute values of V_t at $+V$ and $-V$ increased in the order of AI < BD < ED (**Figure S15** in the Supporting Information). This trend in V_t was translated into the increasing trends of ΔE and Γ (**Figure 4a**). The trends in ΔE and Γ are consistent with the trend of WF and surface coverage, suggesting a coherency between the separate experimental results. Specifically, a higher surface coverage of NHC SAM can cause a larger reduction of the WF of the Au substrate, resulting in a higher ΔE value. Moreover, more chemisorbed NHC molecules per unit area can induce stronger coupling between the molecule and the gold electrode, thereby leading to larger Γ.[21] Based on the values of ΔE and Γ obtained from the TVS analysis, we were able to simulate the trend of S as a function of the deposition condition (**Figure S16** in the Supporting Information). The simulation well reproduced the experimentally observed trend of S (**Figure 4b**). The absolute values of calculated S values were slightly higher than the experimental values, which could be attributed to deviation of Lorentzian shape owing to the thermal fluctuation of the molecules, bias dependence of $T(E)$, and/or intermolecular interaction within SAM, which are not reflected in eq. 2.[64-66]

The molecules within a large-area molecular junction can be considered as resistors in a parallel circuit. As the number of molecules (n) increases, the total resistance of the circuit would linearly decrease. Given this, if the number of molecules increases about 2 times from AI to ED, the current should also increase about 2 times. However, our junction measurements indicate that the current increased by about 100 times as the number of molecules increased by ~2 times from 2.3×10^9 (AI) to 4.4×10^9 (ED). This implies that another factor—the electronic structure of the molecular junction—contributes dominantly to the charge transport property, as discussed above.

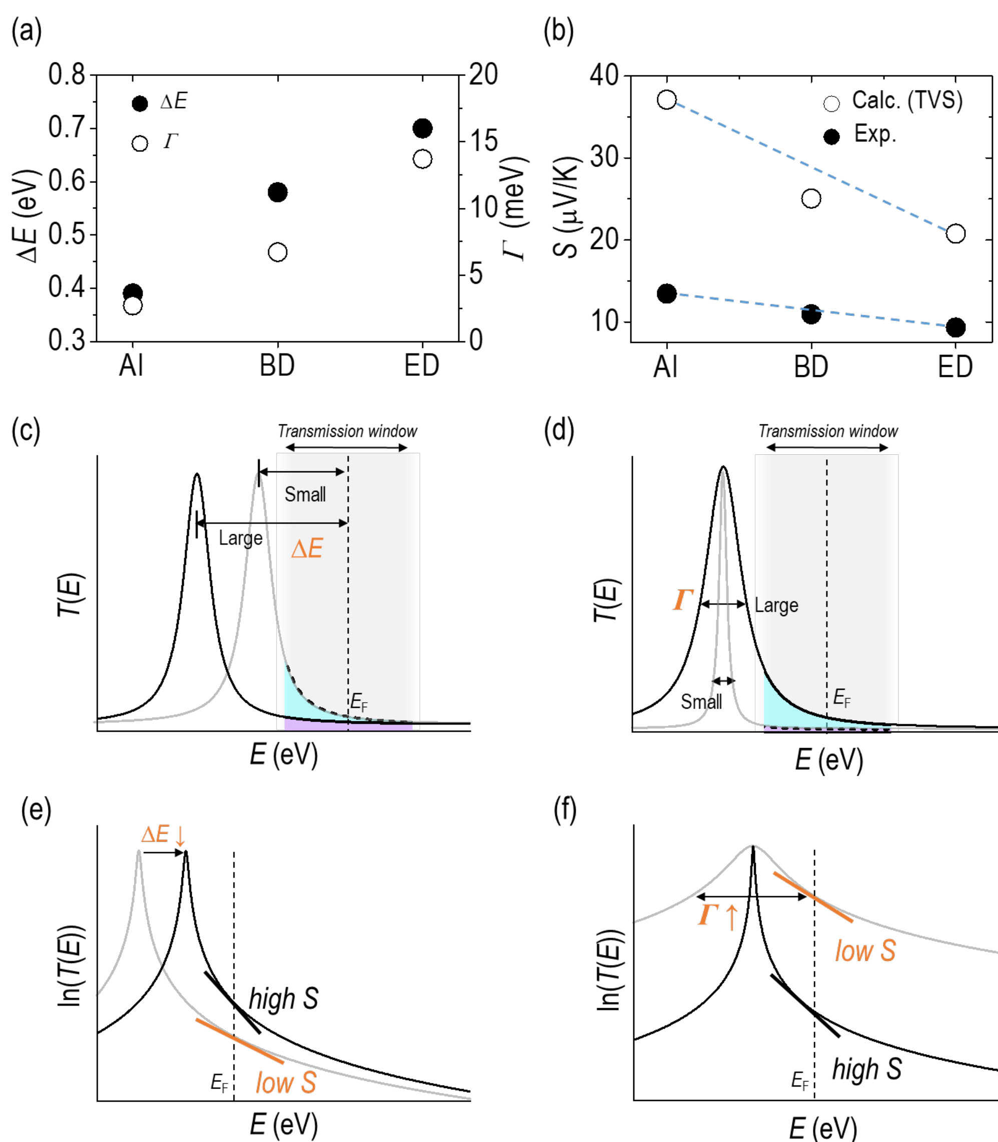

Figure 4. (a) Plots of energy offset (ΔE) between E_F and E_{MO}, and coupling strength (Γ). (b) Comparison of S values obtained by TVS analysis and thermovoltage measurements. Energy level diagrams illustrating the effects of ΔE and Γ on (c, d) tunneling current (the overlap with the transmission window) and (e, f) thermopower of molecular junction.

Interplay of** ΔE**, Γ, J, and S. In this section, we discuss the relationship between the energy barrier shape of NHC junctions and their tunneling and thermoelectric performances. According to the transmission function (Eq. 2), higher ΔE and Γ reduces and increases the overlap between the transmission window and $T(E)$, respectively. This leads to a reduction in tunneling current for higher ΔE (**Figure 4c**) and an increase for higher Γ (**Figure 4d**). However, our experimental results show that the observed trend of J is dominated by Γ, not ΔE. This is similar to observations made by Frisbie and Vilan in thiolate anchor SAMs, where large changes in WF have little influence on ΔE but have significant influence on Γ.[61, 67] The marginal changes in ΔE have been attributed to the strong Fermi level pinning effect[61] while Γ varies exponentially as the extent of work function change increases due to a large induced dipole at the electrode-SAM interface.[67, 68] We assume that the similar Fermi level pinning effect in the NHC anchor also contributes to the dominance of Γ over ΔE. According to the Mott formula (Eq. 3), both increased ΔE and Γ would lower the gradient of $\ln(T(E))$ at E_F (**Figure 4e, f**),[57] which is reconciled with the decreasing trend of S as a function of the deposition conditions from AI to BD and ED.

Power Factor (PF). Lastly, we examined how different deposition conditions affect the power factor (PF) of NHC SAMs. PF is a measure of the power generated by thermoelectric materials under constant temperature differential and calculated as PF = $\sigma \times S^2$, where σ (μS/cm) represents the electrical conductivity. To estimate σ values, we followed the previously reported procedures.[69] The value of σ increased in the order of AI < BD < ED. The σ value for the ED condition was 6.8×10^{-2} μS/cm, which is approximately two orders of magnitude higher than that for the AI condition (3.6×10^{-4} μS/cm). Despite the tradeoff between S and σ, the PF value ($\mu W \cdot m^{-1} \cdot K^{-2}$) increased in the order of AI (6.5×10^{-12}) < BD (8.2×10^{-11}) < ED (5.9×10^{-10}), indicating an enhancement of up to ~10^2 times in PF depending on the deposition condition.[69, 70] It is worth noting that the EGaIn junction usually has a small effective contact area, with the

ratio of effective contact area to geometrical contact area being ~10^{-4}.[71] Thus, taking this account, the PF values can be corrected in the order of ~10^{-8} – ~10^{-6} μW·m^{-1}·K^{-2} (**Figure 5** and **Table 1**).

We further estimated dimensionless figure of merit ($ZT = (\sigma S^2/\kappa)T$) where κ is the thermal conductivity) of the NHC SAM-based junctions. While electrical conductivity and Seebeck coefficient of SAM could be determined by the EGaIn-based junction,[54, 69] measurements of κ of SAM is challenging. Previous study utilizing the time-domain thermoreflectance technique has reported a κ value of 3.6×10^4 μW m^{-1} K^{-1} for SAM composed of dodecanethiolate (SC_{12}).[72] Assuming our NHC SAMs would have the similar κ value, we estimated ZT values of our SAMs: 5.33×10^{-14}, 6.72×10^{-13}, and 4.83×10^{-12} for AI, BD, and ED conditions, respectively. It is noteworthy that the ZT values of BD and ED are ~10 and ~100 times greater than that of SC_{12} SAM (6.6×10^{-14}),[69] respectively. Our experimental design was relevant to singling out the effect of deposition conditions on PF since we used identical bottom substrate (Au^{TS}), top-electrode (conical tip of Ga_2O_3/EGaIn), and molecular backbone (benzo[*d*]imidazole) in all experiments.

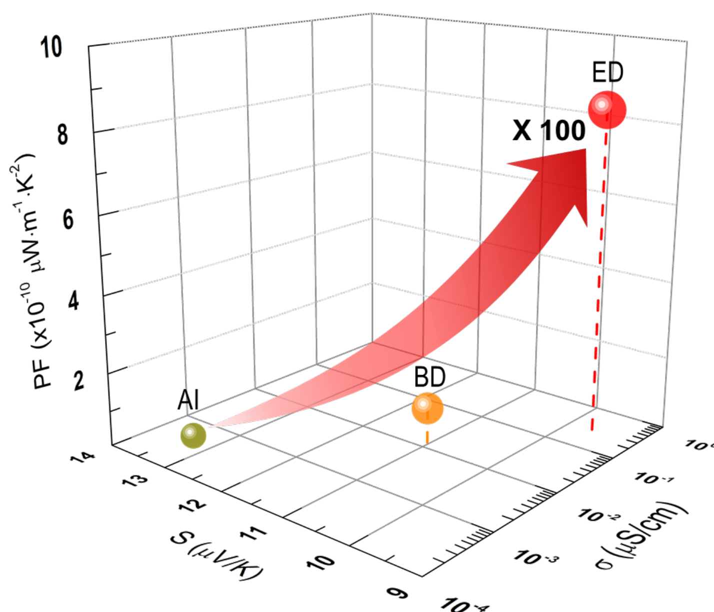

Figure 5. Interplay between power factor (PF), Seebeck coefficient (*S*), and electrical conductivity (σ) of NHC SAMs on Au^{TS} prepared in three different deposition conditions (AI, BD, and ED).

Table 1. Summary of the tunneling conductivity (*σ*), Seebeck coefficient (*S*), and Power Factor (PF) of NHC SAMs depending on the fabrication methods.

SAM	*σ* (μS/cm)	*S* (μV/K)	PF (μW m^{-1} K^{-2})	Corrected PF[a]
AI	3.6×10^{-4}	13.5	6.5×10^{-12}	6.5×10^{-8}
BD	6.9×10^{-3}	10.9	8.2×10^{-11}	8.2×10^{-7}
ED	6.8×10^{-2}	9.3	5.9×10^{-10}	5.9×10^{-6}

[a] The ratio (~10^{-4}) of the effective contact area (A_{eff}) and geometrical contact area (A_{geo}) is reflected.[71]

Conclusion

In summary, our study has investigated the influence of deposition conditions on the electrical and thermoelectric performances of NHC SAM on template-stripped gold substrate. Our findings suggest that the surface coverage of the SAM is mainly determined by the deposition condition, with AI < BD < ED resulting in increasing surface coverage. Further experiments and DFT calculation indicate the strong correlation between surface coverage and work function change of gold electrode. The changes of coverage and work function are directly translated into the changes in the energy barrier shape of junction—energy offset between Fermi level and HOMO energy level and orbital broadening of HOMO caused by the molecule-electrode coupling—which accounts for the opposite trends of current density increases (AI < BD < ED) and Seebeck coefficient (AI > BD > ED) as a function of the deposition condition. Our results lead to the conclusion that the differences in charge transport of NHC SAM depending on the deposition condition is dominated by the orbital broadening, rather than the energy offset. Importantly, we have demonstrated that the power factor of NHC SAM can be significantly improved (up to $\sim 10^2$) by selecting the appropriate deposition condition. Our work provides valuable insights into how deposition conditions impact charge tunneling and thermoelectric performances of large-area junctions based on NHC SAMs.

Acknowledgements

This research was supported by the NRF of Korea (NRF-2019R1A2C2011003, 2019R1A6A1A11044070, 2021M3F3A2A03017999, and 2022R1I1A1A01063120) and JST-PRESTO (Grant Number JPMJPR2115) of Japan. DFT calculations were performed through the use of OCTOPUS at the Cybermedia Center, Osaka University.

References

1. C. A. Smith, M. R. Narouz, P. A. Lummis, I. Singh, A. Nazemi, C.-H. Li and C. M. Crudden, *Chem. Rev.*, 2019, **119**, 4986-5056.

2. C. M. Crudden, J. H. Horton, I. I. Ebralidze, O. V. Zenkina, A. B. McLean, B. Drevniok, Z. She, H.-B. Kraatz, N. J. Mosey, T. Seki, E. C. Keske, J. D. Leake, A. Rousina-Webb and G. Wu, *Nature Chemistry*, 2014, **6**, 409-414.
3. S. Kang, S. E. Byeon and H. J. Yoon, *Bull. Korean Chem. Soc.*, 2021, **42**, 712-723.
4. S. Kang, S. Park, H. Kang, S. J. Cho, H. Song and H. J. Yoon, *Chem. Commun.*, 2019, **55**, 8780-8783.
5. E. A. Doud, M. S. Inkpen, G. Lovat, E. Montes, D. W. Paley, M. L. Steigerwald, H. Vázquez, L. Venkataraman and X. Roy, *J. Am. Chem. Soc.* , 2018, **140**, 8944-8949.
6. A. V. Zhukhovitskiy, M. G. Mavros, T. Van Voorhis and J. A. Johnson, *J. Am. Chem. Soc.*, 2013, **135**, 7418-7421.
7. C. M. Crudden, J. H. Horton, M. R. Narouz, Z. Li, C. A. Smith, K. Munro, C. J. Baddeley, C. R. Larrea, B. Drevniok, B. Thanabalasingam, A. B. McLean, O. V. Zenkina, I. I. Ebralidze, Z. She, H.-B. Kraatz, N. J. Mosey, L. N. Saunders and A. Yagi, *Nat. Commun.*, 2016, **7**, 12654.
8. Z. Tan, J. Liu and W. Hong, *Chem*, 2021, **7**, 2275-2276.
9. X. Xie, P. Li, Y. Xu, L. Zhou, Y. Yan, L. Xie, C. Jia and X. Guo, *ACS Nano*, 2022, **16**, 3476–3505.
10. C. Yang, L. Zhang, C. Lu, S. Zhou, X. Li, Y. Li, Y. Yang, Y. Li, Z. Liu, J. Yang, K. N. Houk, F. Mo and X. Guo, *Nat. Nanotechnol.*, 2021, **16**, 1214-1223.
11. M. Wróbel, T. Żaba, E. Sauter, M. Krawiec, J. Sobczuk, A. Terfort, M. Zharnikov and P. Cyganik, *Adv. Electron. Mater.*, 2021, **7**, 2000947.
12. M.-L. Wang and C.-K. Wang, *Chin. Phys. B*, 2020, **29**, 113101.
13. A. Krzykawska, M. Wróbel, K. Kozieł and P. Cyganik, *ACS Nano*, 2020, **14**, 6043-6057.
14. G. Foti and H. Vázquez, *Nanotechnology*, 2016, **27**, 125702.
15. S. Park, S. Kang and H. J. Yoon, *Nano Lett.*, 2022, **22**, 3953-3960.

16. S. Park, H. Kang and H. J. Yoon, *J. Mater. Chem. A*, 2019, **7**, 14419-14446.

17. S. Engel, E.-C. Fritz and B. J. Ravoo, *Chem. Soc. Rev.*, 2017, **46**, 2057-2075.

18. G. D. Kong and H. J. Yoon, *J. Electrochem. Soc.*, 2016, **163**, G115-G121.

19. L. Srisombat, A. C. Jamison and T. R. Lee, *Colloids Surf. A Physicochem. Eng.*, 2011, **390**, 1-19.

20. C. Vericat, M. E. Vela, G. Benitez, P. Carro and R. C. Salvarezza, *Chem. Soc. Rev.*, 2010, **39**, 1805-1834.

21. A. Inayeh, R. R. K. Groome, I. Singh, A. J. Veinot, F. C. De Lima, R. H. Miwa, C. M. Crudden and A. B. McLean, *Nat. Commun.*, 2021, **12**, 4034

22. K. Chang, J. G. Chen, Q. Lu and M.-J. Cheng, *J. Phys. Chem. A*, 2017, **121**, 2674-2682.

23. K. Chang, J. G. Chen, Q. Lu and M.-J. Cheng, *J. Phys. Chem. C*, 2017, **121**, 24618-24625.

24. B. Adhikari, S. Meng and M. Fyta, *Nanoscale*, 2016, **8**, 8966-8975.

25. J. C. Love, L. A. Estroff, J. K. Kriebel, R. G. Nuzzo and G. M. Whitesides, *Chem. Rev.*, 2005, **105**, 1103-1170.

26. B. D. Gates, Q. Xu, M. Stewart, D. Ryan, C. G. Willson and G. M. Whitesides, *Chem. Rev.*, 2005, **105**, 1171-1196.

27. E. Amit, L. Dery, S. Dery, S. Kim, A. Roy, Q. Hu, V. Gutkin, H. Eisenberg, T. Stein, D. Mandler, F. Dean Toste and E. Gross, *Nat. Commun.*, 2020, **11**, 5714.

28. S. Dery, S. Kim, G. Tomaschun, D. Haddad, A. Cossaro, A. Verdini, L. Floreano, T. Klüner, F. D. Toste and E. Gross, *Eur. J. Chem.* , 2019, **25**, 15067-15072.

29. C.-Y. Wu, W. J. Wolf, Y. Levartovsky, H. A. Bechtel, M. C. Martin, F. D. Toste and E. Gross, *Nature*, 2017, **541**, 511-515.

30. L. Jiang, B. Zhang, G. Médard, A. P. Seitsonen, F. Haag, F. Allegretti, J. Reichert, B. Kuster, J. V. Barth and A. C. Papageorgiou, *Chem. Sci.*, 2017, **8**, 8301-8308.

31. M. Franz, S. Chandola, M. Koy, R. Zielinski, H. Aldahhak, M. Das, M. Freitag, U. Gerstmann, D. Liebig, A. K. Hoffmann, M. Rosin, W. G. Schmidt, C. Hogan, F. Glorius, N. Esser and M. Dähne, *Nat. Chem.*, 2021, **13**, 828-835.
32. G. Wang, A. Rühling, S. Amirjalayer, M. Knor, J. B. Ernst, C. Richter, H.-J. Gao, A. Timmer, H.-Y. Gao, N. L. Doltsinis, F. Glorius and H. Fuchs, *Nat. Chem.*, 2017, **9**, 152-156.
33. H. J. Yoon, K.-C. Liao, M. R. Lockett, S. W. Kwok, M. Baghbanzadeh and G. M. Whitesides, *J. Am. Chem. Soc.*, 2014, **136**, 17155-17162.
34. G. D. Kong, S. E. Byeon, J. Jang, J. W. Kim and H. J. Yoon, *J. Am. Chem. Soc.*, 2022, **144**, 7966-7971.
35. G. D. Kong, H. Song, S. Yoon, H. Kang, R. Chang and H. J. Yoon, *Nano Lett.*, 2021, **21**, 3162-3169.
36. R. C. Chiechi, E. A. Weiss, M. D. Dickey and G. M. Whitesides, *Angew. Chem. Int. Ed.*, 2008, **47**, 142-144.
37. H. V. Huynh, T. T. Lam and H. T. T. Luong, *RSC Adv.*, 2018, **8**, 34960-34966.
38. A. Jablonski and C. J. Powell, *J Electron Spectros Relat Phenomena.*, 2017, **218**, 1-12.
39. K. Tamada, T. Ishida, W. Knoll, H. Fukushima, R. Colorado, M. Graupe, O. E. Shmakova and T. R. Lee, *Langmuir*, 2001, **17**, 1913-1921.
40. I. Zaccari, B. G. Catchpole, S. X. Laurenson, A. G. Davies and C. Wälti, *Langmuir*, 2014, **30**, 1321-1326.
41. E. Boubour and R. B. Lennox, *Langmuir*, 2000, **16**, 4222-4228.
42. N. Metoki, L. Liu, E. Beilis, N. Eliaz and D. Mandler, *Langmuir*, 2014, **30**, 6791-6799.
43. R. K. Shervedani and S. A. Mozaffari, *Anal. Chim. Acta*, 2006, **562**, 223-228.
44. T. M. Nahir and E. F. Bowden, *Electrochim. Acta*, 1994, **39**, 2347-2352.
45. A. Lasia and A. Rami, *J. Electroanal. Chem.*, 1990, **294**, 123-141.

46. G. D. Kong, M. Kim, S. J. Cho and H. J. Yoon, *Angew. Chem. Int. Ed.*, 2016, **55**, 10307-10311.
47. M. H. Schoenfisch and J. E. Pemberton, *J. Am. Chem. Soc.*, 1998, **120**, 4502-4513.
48. H. K. Kim, A. S. Hyla, P. Winget, H. Li, C. M. Wyss, A. J. Jordan, F. A. Larrain, J. P. Sadighi, C. Fuentes-Hernandez, B. Kippelen, J.-L. Brédas, S. Barlow and S. R. Marder, *Chem. Mater.*, 2017, **29**, 3403-3411.
49. N. Gozlan, U. Tisch and H. Haick, *J. Phys. Chem. C*, 2008, **112**, 12988-12992.
50. T. Abu-Husein, S. Schuster, D. A. Egger, M. Kind, T. Santowski, A. Wiesner, R. Chiechi, E. Zojer, A. Terfort and M. Zharnikov, *Adv. Func. Mater.*, 2015, **25**, 3943-3957.
51. M. Gärtner, E. Sauter, G. Nascimbeni, A. Petritz, A. Wiesner, M. Kind, T. Abu-Husein, M. Bolte, B. Stadlober, E. Zojer, A. Terfort and M. Zharnikov, *J. Phys. Chem. C*, 2018, **122**, 28757-28774.
52. S. Park, J. Jang, H. Kim, D. I. Park, K. Kim and H. J. Yoon, *J. Mater. Chem. A*, 2020, **8**, 19746-19767.
53. S. Park and H. J. Yoon, *ACS Appl. Mater. Interfaces*, 2022, **14**, 22818-22825.
54. S. Park and H. J. Yoon, *Nano Lett.*, 2018, **18**, 7715-7718.
55. P. Reddy, S.-Y. Jang, R. A. Segalman and A. Majumdar, *Science*, 2007, **315**, 1568-1571.
56. J. Jang, P. He and H. J. Yoon, *Acc. Chem. Res.*, 2023, **56**, 1613-1622.
57. S. Park, J. Jang and H. J. Yoon, *J. Phys. Chem. C*, 2021, **125**, 20035-20047.
58. H. B. Michaelson, *J. Appl. Phys.*, 1977, **48**, 4729-4733.
59. E. J. Lous, P. W. M. Blom, L. W. Molenkamp and D. M. De Leeuw, *J. Appl. Phys.*, 1997, **81**, 3537-3542.
60. J. M. Beebe, B. Kim, J. W. Gadzuk, C. Daniel Frisbie and J. G. Kushmerick, *Phys. Rev. Lett.*, 2006, **97**, 026801.
61. Z. Xie, I. Bâldea and C. D. Frisbie, *J. Am. Chem. Soc.*, 2019, **141**, 3670-3681.

62. Z. Xie, I. Bâldea and C. D. Frisbie, *J. Am. Chem. Soc.*, 2019, **141**, 18182-18192.

63. Q. V. Nguyen, Z. Xie and C. D. Frisbie, *J. Phys. Chem. C*, 2021, **125**, 4292-4298.

64. M. A. Ochoa and M. Zwolak, *Chem. Phys.*, 2019, **150**, 141102.

65. J. Jang, G. D. Kong, H. Kang and H. J. Yoon, *J. Phys. Chem. C*, 2023, **127**, 6025–6033.

66. R. Yamada, K. Albrecht, T. Ohto, K. Minode, K. Yamamoto and H. Tada, *Nanoscale*, 2018, **10**, 19818-19824.

67. A. Vilan, D. Aswal and D. Cahen, *Chem. Rev.*, 2017, **117**, 4248-4286.

68. B. Kim, S. H. Choi, X. Y. Zhu and C. D. Frisbie, *J. Am. Chem. Soc.*, 2011, **133**, 19864-19877.

69. S. Park, S. Kang and H. J. Yoon, *ACS Cent. Sci.*, 2019, **5**, 1975-1982.

70. W. Peng, Z. Cao, N. Chen, Y. Xie and Y. Li, *J. Mater. Chem. A*, 2022, **10**, 23304-23313.

71. F. C. Simeone, H. J. Yoon, M. M. Thuo, J. R. Barber, B. Smith and G. M. Whitesides, *J. Am. Chem. Soc.*, 2013, **135**, 18131-18144.

72. M. D. Losego, M. E. Grady, N. R. Sottos, D. G. Cahill and P. V. Braun, *Nat. Mater.*, 2012, **11**, 502-506.